Available online at www.sciencedirect.com
ScienceDirect
Trans. Nonferrous Met. Soc. China 31(2021) 265−276
Transactions of Nonferrous Metals Society of China
www.tnmsc.cn

Microemulsion synthesis of $ZnMn_2O_4/Mn_3O_4$ sub-microrods for Li-ion batteries and their conversion reaction mechanism

Ting-ting FENG, Jian YANG, Si-yi DAI, Jun-chao WANG, Meng-qiang WU

School of Materials and Energy, University of Electronic Science and Technology of China, Chengdu 611731, China

Received 16 January 2020; accepted 10 December 2020

Abstract: The hierarchical $ZnMn_2O_4/Mn_3O_4$ composite sub-microrods were synthesized via a water-in-oil microemulsion method followed by calcination. The $ZnMn_2O_4/Mn_3O_4$ electrode displays an intriguing capacity increasing from 440 to 910 mA·h/g at 500 mA/g during 550 consecutive discharge/charge cycles, and delivers an ultrahigh capacity of 1276 mA·h/g at 100 mA/g, which is much greater than the theoretical capacity of either $ZnMn_2O_4$ or Mn_3O_4 electrode. To investigate the underlying mechanism of this phenomenon, cyclic voltammetry and differential capacity analysis were applied, both of which reveal the emergence and the growth of new reversible redox reactions upon charge/discharge cycling. The new reversible conversions are probably the results of an activation process of the electrode material during the cycling process, leading to the climbing charge storage. However, the capacity exceeding the theoretical value indicates that there are still other factors contributing to the increasing capacity.

Key words: $ZnMn_2O_4/Mn_3O_4$ sub-microrods; microemulsion; conversion reaction mechanism; cyclic voltammetry; differential capacity analysis

1 Introduction

The ever-increasing need for higher energy densities at lower costs, has prompted extensive research activities on the development of novel electrode materials for lithium ion batteries (LIBs), which are widely used in electric products ranging from portable electronics to electric vehicles. In recent years, the metal oxides with high theoretical reversible energy capacities have attracted increasing attention and are studied as the next-generation anode materials for high-performance LIBs. In particular, manganese-based oxides MnO_x including MnO, Mn_2O_3, Mn_3O_4, MnO_2 [1−5], and the bimetallic oxides like $ZnMn_2O_4$, $NiMn_2O_4$ and $CoMn_2O_4$ [6−8] etc., are of significant interest due to their high energy storage capacities, low conversion voltages, small potential hystereses, low costs and environmental friendliness.

Among the bimetallic Mn-based oxides, $ZnMn_2O_4$ becomes very popular in the research field. To improve the electrochemical properties of $ZnMn_2O_4$, great efforts have been devoted to synthesis methods, micro/nano-structure design, material modification and compounding, etc. For example, ZHANG et al [9] reported that hydrothermally synthesized porous $ZnMn_2O_4$ nanowires maintained a high reversible capacity of 869.5 mA·h/g at a current density of 500 mA/g after 100 cycles, and delivered a specific capacity of 345.4 mA·h/g even at a high current density of 4000 mA/g. LIU et al [10] successfully devised a facile polyol-based method to synthesize quasi-mesocrystal $ZnMn_2O_4$ porous twin-microspheres with remarkable lithium storage properties, which delivered a capacity of 1084 mA·h/g at 0.2 A/g over 190 cycles.

Corresponding author: Ting-ting FENG, Tel: +86-15828627671, E-mail: fengtt@uestc.edu.cn;
Meng-qiang WU, Tel: +86-13072808258, E-mail: mwu@uestc.edu.cn
DOI: 10.1016/S1003-6326(21)65493-6

Although being extensively studied, the intrinsic conversion mechanism of $ZnMn_2O_4$ has not been discussed in depth, and a generally fixed understanding has been formed. As revealed by YANG et al [11], $ZnMn_2O_4$ is reduced to LiZn alloy and metallic Mn^0 embedded in amorphous Li_2O matrix after the first lithiation, and the reductive products are then oxidized to MnO and ZnO after the first delithiation, as indicated by their CV result. Therefore, the corresponding theoretical reversible capacity of $ZnMn_2O_4$ is calculated to be 784 mA·h/g. However, KIM et al [12] found one additional anodic peak near 2.2 V appeared at the first delithiation scan for their pure $ZnMn_2O_4$ nanowires, and also identified the formation of Mn_3O_4 and ZnO phases by ex situ X-ray diffraction (XRD) and transmission electron microscopy (TEM) studies after the initial discharge/charge cycle. These results indicate that an additional oxidation step of MnO to Mn_3O_4 occurred during the delithiation. The similar problem also exists in the MnO_x anode materials. It is generally believed that MnO_x electrode materials storage and release electron charges via reversible redox reactions that only involve metallic Mn^0 and MnO, as indicated by many CV results. Moreover, MnO was also identified as the final phase at the cutoff voltage (3.0 V) for Mn_2O_3 and Mn_3O_4 electrodes by operando X-ray diffraction and X-ray absorption spectroscopy studies [13,14]. However, there are still a few studies revealing a different result [15−17]. For example, DENG et al [17] observed a pair of redox peaks (a cathodic peak at 1.25 V and an anodic peak at 2.35 V) correlated with the conversion between Mn^{2+} and Mn^{3+} in their Mn_2O_3 microsphere anode in the first three consecutive CV cycles. Therefore, there is a question about the final phase of the Mn-based oxides after delithiation and the intrinsic conversion mechanism should be further studied.

In addition, the phenomena of the capacity increasing during discharge/charge cycling and the capacity exceeding the theoretical values of $ZnMn_2O_4$ and MnO_x electrodes were observed in some studies [15,18−20], which also raise questions about the previous understanding of the conversion reaction mechanism for the Mn-based oxides and suggest the existence of additional contributions to the capacity in the discharge/charge process. Therefore, further investigations are still needed to find out the conversion reaction mechanism of the Mn-based oxide electrode materials, especially the final valence state of the Mn ions after delithiation, as well as other capacity contributors.

In this work, we make use of CV measurements and differential capacity analysis to investigate the conversion mechanism of the micro-emulsion synthesized $ZnMn_2O_4/Mn_3O_4$ composite sub-microrod material, which showed a continuous increase in charge storage capacity and an ultrahigh capacity exceeding the theoretical value. The results disclose the emergence and the enhancement of new redox conversions upon cycling could explain the growing discharge/charge capacity.

2 Experimental

2.1 Material synthesis

A microemulsion synthesis and a calcination process were used to obtain the hierarchical $ZnMn_2O_4/Mn_3O_4$ composite sub-microrods. In a typical synthesis, 3 g of hexadecyltrimethyl-ammonium bromide (CTAB) and 5 mL of *n*-pentanol were added in 100 mL of cyclohexane to form a milky emulsion. 5 mL of oxalic acid ($H_2C_2O_4$, 3 mmol) aqueous solution was then dripped in under magnetic stirring. After stirring for 30 min, 5 mL of Millipore water (18 MΩ) containing 0.25 mmol of $Zn(NO_3)_2·6H_2O$ and 0.5 mmol $MnCl_2·4H_2O$ was added dropwise. The reaction was allowed to proceed for 12 h under continuous stirring before the precipitates were collected, washed with ethanol and DI water several times and dried at 80 °C overnight. The white product was finally calcined in a quartz tube at 600 °C for 6 h under air using a heating rate of 5 °C/min.

2.2 Material characterization

The obtained materials were characterized with field-emission scanning electron microscopy (FESEM, Hitachi S4700), X-ray diffraction (XRD, Siemens/Bruker D-5000 and Philips X'pert), transmission electron microscope (TEM, JEOL 2100) and X-ray photoelectron spectroscopy (XPS, Kratos Axis ULTRA).

2.3 Electrochemical measurement

The electrochemical properties of the $ZnMn_2O_4/Mn_3O_4$ sub-microrods were investigated

using 2032 coin-type cells with metallic lithium as the counter and reference electrode and 1 mol/L $LiPF_6$ in a mixture of ethylene carbonate and diethyl carbonate (1:1 by mass ratio) solution as the electrolyte. The working electrodes were prepared by coating the mixture of 70 wt.% active material, 20 wt.% conductive carbon black (Super-P) and 10 wt.% polymer binder (carboxyl methyl cellulose, CMC) on aluminum foil as the current collector. Coin-cell batteries were assembled in an Ar-filled glovebox with moisture and oxygen concentrations below 1.0×10^{-6} and tested on a BioLogic BCS battery cycling system. The cyclic voltammograms were measured in a potential range of 0.01−3.0 V (vs Li^+/Li). The galvanostatic discharge/charge measurements were performed at current densities ranging from 100 to 2000 mA/g over a voltage range of 0.01−3.0 V.

3 Results and discussion

3.1 Synthesis mechanism and material characterization

Figure 1(a) shows the schematic diagram of the synthesis procedure for the precursor of the $ZnMn_2O_4/Mn_3O_4$ sub-microrods that are obtained via an oxalate co-precipitation method in a water-in-oil microemulsion using CTAB as the structure-directing agent. The evolution and the structure-directing mechanism of the CTAB templates are also illustrated in Fig. 1(b). After the addition of oxalic acid aqueous solution, a colorless and transparent quaternary water-in-oil micro-emulsion of cyclohexane, *n*-pentanol, water and CTAB is formed. The amphipathic CTAB molecules are self-assembled into high-aspect-ratio nanorods at the water/oil interface, which further aggregate into sub-microrod micelles with various lengths and diameters. The addition of the $Zn(NO_3)_2\cdot6H_2O$ and $MnCl_2\cdot4H_2O$ aqueous solution into the microemulsion solution immediately initiates the coprecipitation reaction and the formation of the Zn/Mn oxalate. Since the reaction is restricted to the water microphases, the obtained Zn/Mn oxalate precipitates are therefore confined within the CTAB sub-microrod micelle templates, leading to a similar sub-microrod structure. This synthesis mechanism is further confirmed by the microstructure and phase characterizations of the obtained materials.

Figures 2(a) and (b) display the SEM images of the microemulsion-synthesized precursor before calcination, which exhibit a microstructure of solid rectangular columns with a length of 1−10 μm and a diameter of 0.1−1 μm. The corresponding XRD in Fig. 2(c) reveals that the microemulsion-synthesized precursor is composed of two mixed phases of $ZnC_2O_4\cdot2H_2O$ (JCPDS No. 00-025-1029) and $MnC_2O_4\cdot2H_2O$ (JCPDS No. 00-057-0602). After calcination in air, the final product maintains the feature of rectangular columns (as presented in Fig. 2(d)), but displays a hierarchical structure consisting of nanoparticles with an average diameter of about 30 nm (Fig. 2(e)). Figure 2(f) presents the XRD pattern of the sintered sample. The diffraction peaks can be indexed to hetaerolite $ZnMn_2O_4$

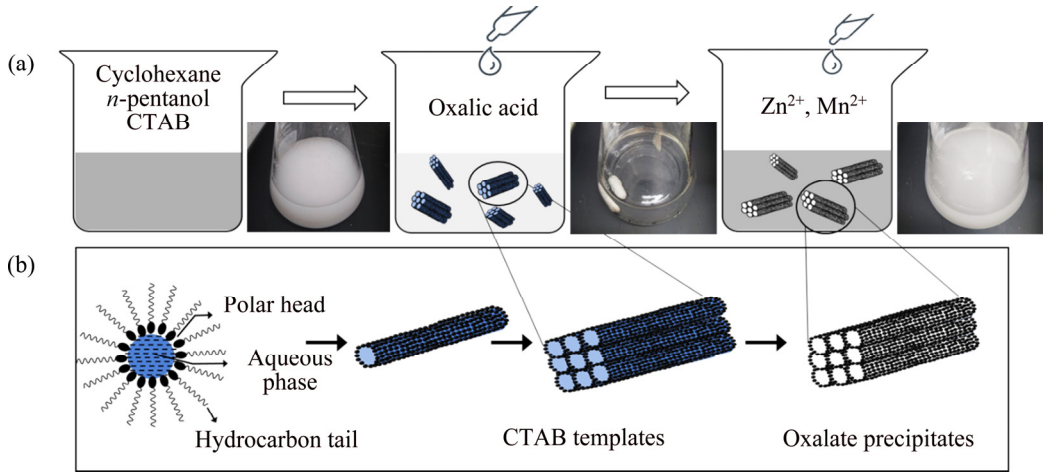

Fig. 1 Schematic diagram of synthesis procedure for precursor of $ZnMn_2O_4/Mn_3O_4$ composite sub-microrods (a) and proposed formation and structure-directing process of CTAB templates (b)

(JCPDS No. 00-24-1133) and manganese oxide Mn_3O_4 (JCPDS No. 00-13-0162). Quantitative analysis of the XRD pattern indicates the phase compositions of $ZnMn_2O_4$ and Mn_3O_4 are 61.6 wt.% and 38.4 wt.%, respectively.

Based on the above results, the growth mechanism of the microemulsion-synthesized and CTAB-templated $ZnMn_2O_4/Mn_3O_4$ composite sub-microrods can be described as follows:

$$Zn^{2+} + C_2O_4^{2-} + 2H_2O \rightarrow ZnC_2O_4 \cdot 2H_2O \quad (1)$$

$$Mn^{2+} + C_2O_4^{2-} + 2H_2O \rightarrow MnC_2O_4 \cdot 2H_2O \quad (2)$$

$$ZnC_2O_4 \cdot 2H_2O + MnC_2O_4 \cdot 2H_2O \xrightarrow[600\ ^\circ C,\ 6\ h]{Air} ZnMn_2O_4 + Mn_3O_4 \quad (3)$$

Figures 3(a, b) present the TEM images of the $ZnMn_2O_4/Mn_3O_4$ sub-microrods, which further confirm that the microemulsion-synthesized $ZnMn_2O_4/Mn_3O_4$ product is a rod-like structure composed of nanoparticles with diameters around 20−30 nm, as exhibited in Fig. 3(b), which is consistent with the SEM result. Figure 3(c) shows a high-resolution image of one nanoparticle with clear lattice fringes, and the spacing of 0.286 nm is corresponding to the (200) plane of hetaerolite $ZnMn_2O_4$. XPS is used to examine the surface elements and their chemical bonding states of the $ZnMn_2O_4/Mn_3O_4$ composite sub-microrods, and the results are shown in Fig. 4. The survey spectrum in Fig. 4(a) shows the existence of Zn, Mn, O and C (always present). The HR-XPS spectrum of Zn $2p_{3/2}$ subpeak is presented in Fig. 4(b) with a binding energy of 1020.6 eV, indicating the presence of Zn^{2+}. Figure 4(c) shows Mn $2p_{1/2}$ and Mn $2p_{3/2}$ subpeaks centered at 653.4 and 641.6 eV, respectively, and

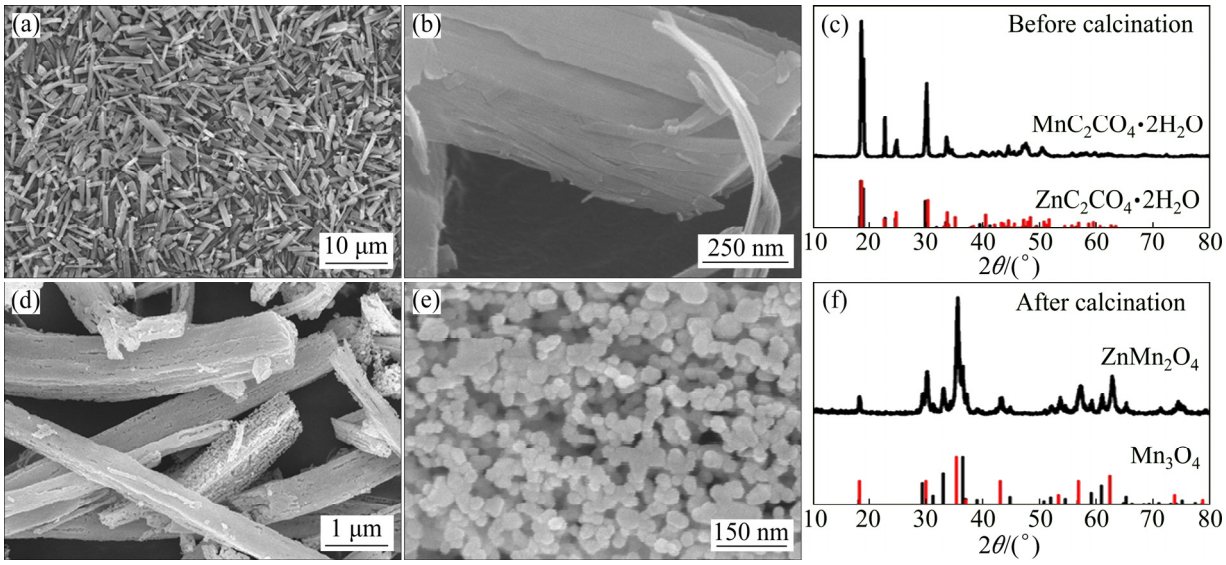

Fig. 2 SEM images (a, b) and XRD pattern (c) of precursor before sintering, and SEM images (d, e) and XRD pattern (f) of $ZnMn_2O_4/Mn_3O_4$ composite sub-microrods

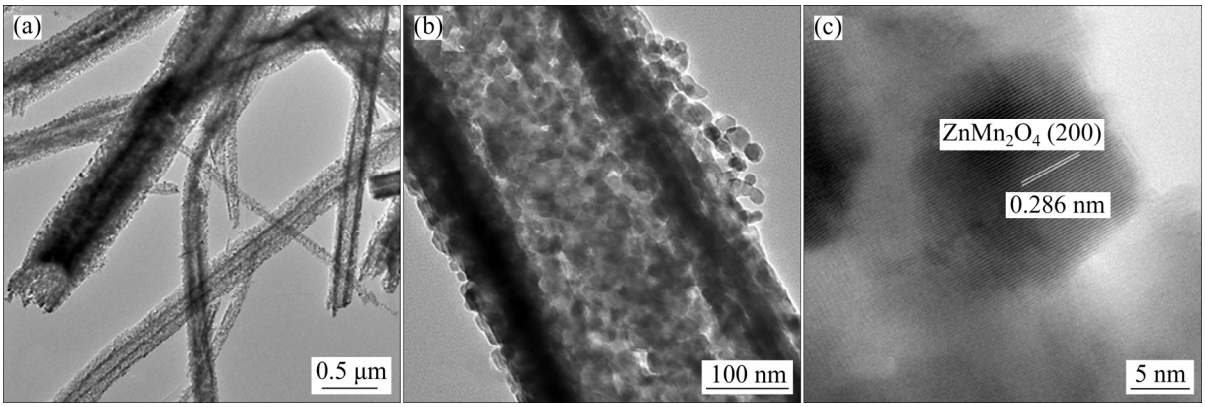

Fig. 3 TEM images (a, b) of $ZnMn_2O_4/Mn_3O_4$ composite sub-microrods at various magnifications and HRTEM image of one nanoparticle (c)

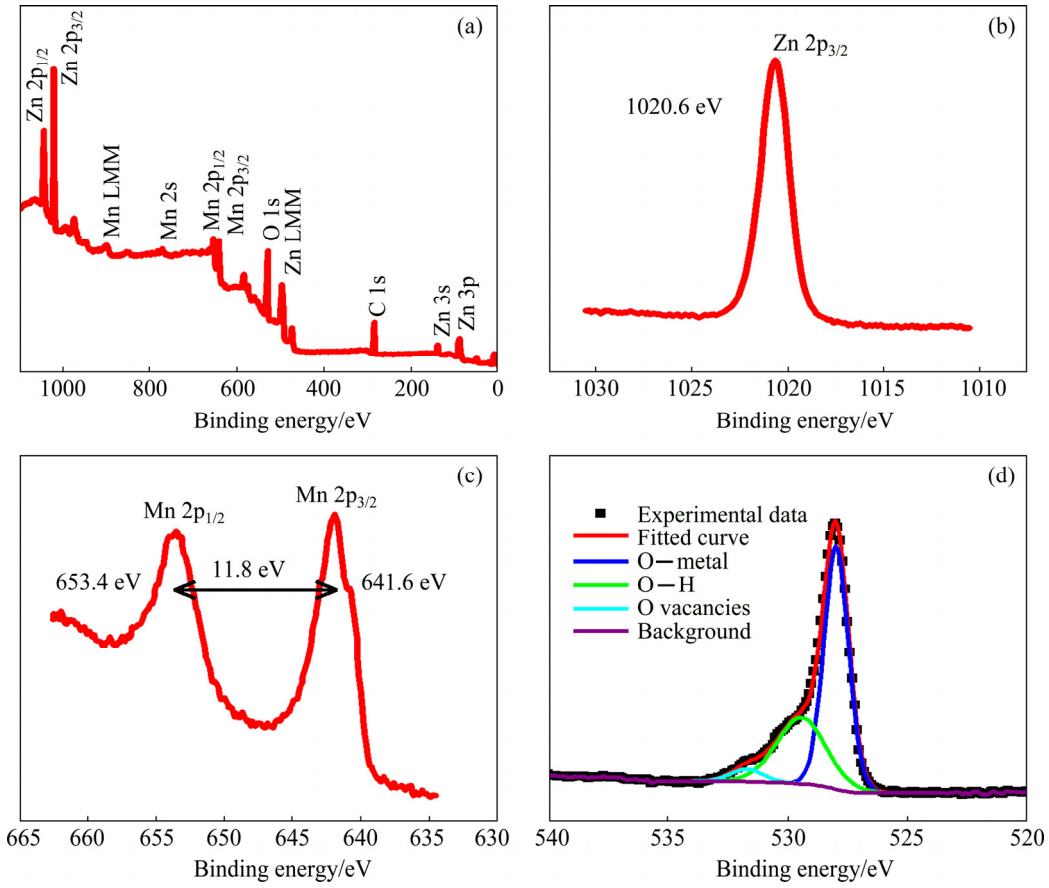

Fig. 4 XPS spectra of $ZnMn_2O_4/Mn_3O_4$ composite sub-microrods: (a) XPS survey scan; (b) Zn $2p_{3/2}$; (c) Mn $2p_{1/2}$ and $2p_{3/2}$; (d) O 1s

the spin-energy separation between the two subpeaks is 11.8 eV, which is the characteristic of Mn_3O_4 [21]. The HR-XPS spectrum of O 1s in Fig. 4(d) has been deconvoluted to three components. The peaks located at 529.5 and 533.2 eV can be assigned to the lattice oxygen of metal oxide and the O—H species for residual water, while the one at 531.0 eV may be attributable to the oxygen vacancies within the metal oxides [22,23].

3.2 Electrochemical performance and analysis

3.2.1 Electrochemical properties of $ZnMn_2O_4/Mn_3O_4$ anode

The electrochemical properties of the $ZnMn_2O_4/Mn_3O_4$ composite material are characterized using 2032-type coin cells. Figure 5(a) shows the CV profiles of a typical cell with the first three cycles at a scanning speed of 0.2 mV/s, which agrees well with the previous studies [11,20,24]. The appearance a of weak and broad cathodic peak at around 1.0 V in the first lithiation process can be attributed to the SEI formation and the reduction from Mn_3O_4 to MnO, while the significant peak at around 0.18 V (vs Li^+/Li) could be assigned to the reduction of MnO and ZnO to metallic Mn^0 and Zn^0 nanograins, and the formation of a LiZn alloy. Therefore, the initial lithiation process of $ZnMn_2O_4$ and Mn_3O_4 could be explained as follows [24−26]:

$$ZnMn_2O_4+8Li^++8e\rightarrow Zn+2Mn+4Li_2O \quad (4)$$

$$Mn_3O_4+8Li^++8e\rightarrow 3Mn+4Li_2O \quad (5)$$

$$Zn+Li^++e\rightarrow ZnLi \quad (6)$$

The subsequent lithiation scans are quite different from the initial one, and only one defined reduction peak is observed at around 0.5 V, indicating that irreversible reactions happen during the first scan. However, the three delithiation curves overlap each other, with one weak peak at approximately 0.3 V related to the dealloying of LiZn, and the following two oxidation peaks around 1.2 and 1.5 V corresponding to the oxidation of Mn^0 and Zn^0 to MnO and ZnO, respectively. The second

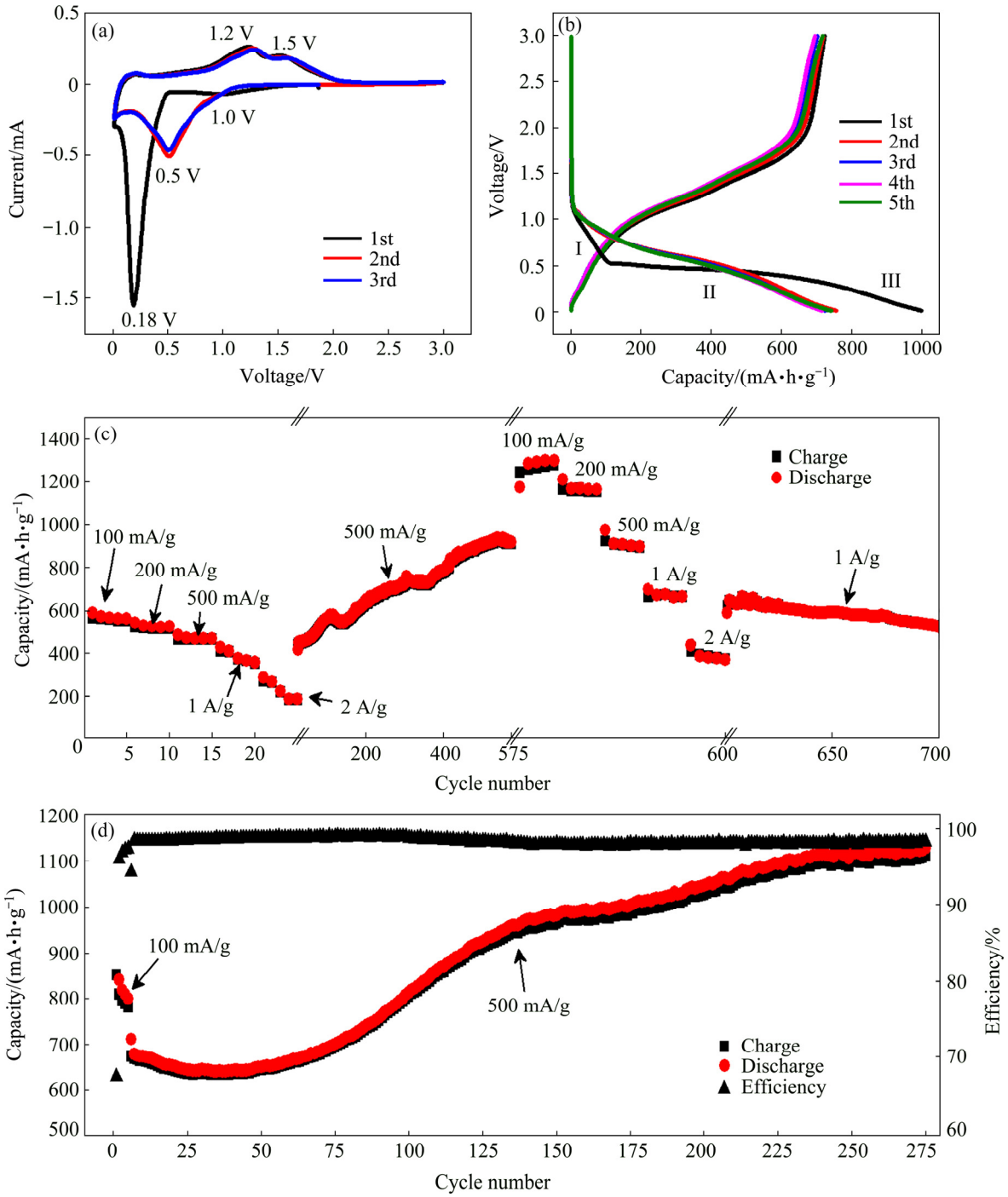

Fig. 5 Typical CV profiles of $ZnMn_2O_4/Mn_3O_4$ sub-microrod electrode (a), the first five cycles of galvanostatic discharge/charge curves of one half-cell (b), cycling performance of Cell 1 after 3 cycles of CV scans (c), and cycling performance of Cell 2 at 500 mA/g after five cycles at 100 mA/g (d)

and the third CV curves coincide very well with each other, indicating a good reversibility of the $ZnMn_2O_4/Mn_3O_4$ composite electrode.

According to the CV profiles, the reversible redox reactions of the $ZnMn_2O_4/Mn_3O_4$ composite electrode are concluded as

$$ZnLi \rightleftharpoons Zn+Li^{+}+e \quad (7)$$

$$Zn+Li_2O \rightleftharpoons ZnO+2Li^{+}+2e \quad (8)$$

$$Mn+Li_2O \rightleftharpoons MnO+2Li^{+}+2e \quad (9)$$

As discussed before, the final phases of the $ZnMn_2O_4/Mn_3O_4$ composite at the end of the delithiation are ZnO and MnO in view of the CV result. In other words, Mn^{3+} will be irreversibly reduced to Mn^{2+} during the first lithiation process.

This conversion reaction has also been observed in many other Mn-based oxides, such as Mn_2O_3 and Mn_3O_4.

Figure 5(b) shows the first five cycles of the galvanostatic discharge/charge profiles of a typical cell. A specific capacity of ~1000 mA·h/g is obtained in the first discharge process, while only 722 mA/g is delivered for the first charge process, giving rise to an initial coulombic efficiency of 72.2%. The successive discharge/charge profiles coincide well with each other and exhibit a reversible lithiation/delithiation process of the $ZnMn_2O_4/Mn_3O_4$ electrode.

Figure 5(c) shows the discharge/charge capacities of a half-cell after three cycles of CV test (denoted by Cell 1). The cell is cycled at 100, 200, 500, 1000 and 2000 mA/g in a stepwise fashion over the first 25 cycles, delivering average capacities of 555, 516, 464, 383 and 223 mA·h/g, respectively. The cell is then cycled at 500 mA/g for the successive 550 cycles, and the charge storage capacity of the $ZnMn_2O_4/Mn_3O_4$ sub-microrod electrode is first recovered to 440 mA·h/g and then gradually climbs to ~910 mA·h/g, which greatly exceeds the theoretical reversible capacity of the $ZnMn_2O_4/Mn_3O_4$ composite (753 mA·h/g, according to the mass ratio of the $ZnMn_2O_4/Mn_3O_4$ composite and their theoretical values). This observation is strikingly different from the behaviors of most active materials for LIBs, which generally experience a capacity fading upon cycling. After that, the cell is again cycled at 100 mA/g for 5 cycles, and delivers an ultrahigh capacity of 1276 mA·h/g. When the discharge/charge current density is again increased to 200, 500, 1000 and 2000 mA/g, the capacity remains high at 1155, 908, 670 and 493 mA·h/g, respectively. The cell is then cycled at 1000 mA/g for another 100 cycles, and the capacity of 523 mA·h/g is obtained even after a total of 700 discharge/charge cycles, demonstrating good cycling performance of the $ZnMn_2O_4/Mn_3O_4$ composite sub-microrods as an anode material for LIBs.

The increase of the reversible lithium storage capacity with cycling is typically observed in our $ZnMn_2O_4/Mn_3O_4$ composite electrodes. Figure 5(d) shows another half-cell (Cell 2) which is cycled 270 times at 500 mA/g following 5 cycles at 100 mA/g. As can be seen, after a slight drop for the first 30 cycles, the charge storage progressively rises from 632 to 1127 mA/g during the subsequent 240 cycles, which also exceeds the theoretical capacity. The columbic efficiency remains nearly stable at 98.5% except for the first several cycles.

3.2.2 Conversion reaction mechanism

To find out the specific reasons for the continuous capacity growth and its exceeding theoretical value, we monitored the redox reaction changes of the $ZnMn_2O_4/Mn_3O_4$ electrode at different discharge/charge cycles by CV technique along with differential capacity analysis.

(1) CV analysis

Figure 6 shows the CV curves at a scan rate of 0.1 mV/s obtained from one typical $ZnMn_2O_4/Mn_3O_4$ half-cell before cycling, after 50 and 100 galvanostatic discharge/charge cycles at 500 mA/g. Each CV test is scanned for three cycles to ensure the coincidence of the CV curves. A distinct change is shown in the CV curves after cycling, compared to the initial curve. A pair of new redox peak appears with the anodic peak located at around 2.2 V and the cathodic peak at around 1.2 V, as indicated by the two short arrows, which suggest the occurrence of a new pair of redox conversion reactions. As discussed before, the $ZnMn_2O_4/Mn_3O_4$ composite material would transform into MnO and ZnO during delithiation, corresponding to the two anodic peaks at around 1.2 and 1.5 V. Therefore, the new redox conversion emerged at 2.2 V could only be associated with MnO, which could be further oxidized. According to the findings of previous research on the oxidation mechanism of Mn/MnO film, Mn^0 will go through four oxidation steps from (1) Mn^0 to MnO, (2) from MnO to Mn_3O_4, (3) from Mn_3O_4 to Mn_2O_3, and (4) from Mn_2O_3 to MnO_2, and each oxidation corresponds to an oxidation peak in the CV curves [27]. Therefore, the new oxidation reaction at 2.2 V is most likely attributed to the oxidation conversion from MnO to Mn_3O_4, which could be described as

$$3MnO+Li_2O \rightleftharpoons Mn_3O_4+2Li^++2e \quad (10)$$

Actually, the pure MnO materials in our previous study [28] and the work of GU et al [16] also exhibit two well defined oxidation peaks at around 1.3 and 2.2 V during the first anodic scan, which demonstrates that the reversible conversion of MnO and Mn_3O_4 could happen during the anodic process, even the starting electrode material is MnO. The difference is that the oxidation of MnO

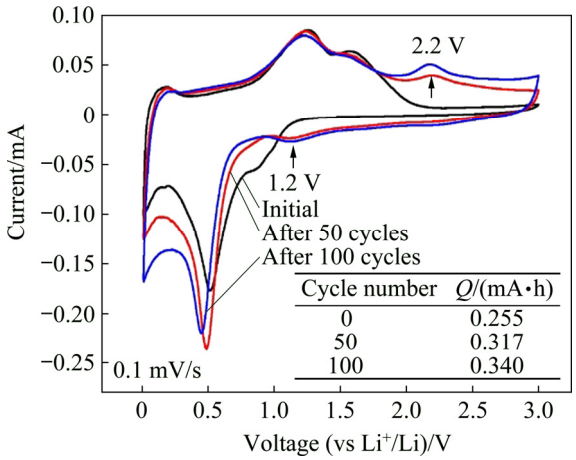

Fig. 6 CV curves of typical $ZnMn_2O_4/Mn_3O_4$ half-cell before galvanostatic discharge/charge cycling, after 50 cycles and 100 cycles

to Mn_3O_4 becomes obvious after several dozens of galvanostatic discharge/charge cycles in our study, while it appears at the first beginning in the other studies.

In addition, according to the CV plots, the peak intensity increases with cycling, indicating the enhancement of the MnO/Mn_3O_4 redox conversion. The charge capacities obtained from the CV curves at different cycles are illustrated in the inset of Fig. 6, revealing the incremental capacity of the $ZnMn_2O_4/Mn_3O_4$ electrode with cycling. Therefore, it is proved that the appearance and the enhancement of the reversible redox conversion between MnO and Mn_3O_4 is (at least partly) responsible for the capacity increase upon cycling.

(2) Differential capacity analysis

To learn more about the conversion mechanism of our $ZnMn_2O_4/Mn_3O_4$ electrode, the differential capacity analysis (dQ/dV) based on galvanostatic discharge/charge cycling curves was carried out. Figure 7(a) shows the first five cycles of the dQ/dV vs V curves derived from Fig. 5(b), which coincide with each other well except for the first cycle. Mathematically, peaks in the dQ/dV curves reflect the voltage plateaus during the discharge/charge processes, hence they can trace the occurrence of the redox reactions. When comparing the dQ/dV plot with the CV curves shown in Fig. 7(b), it is found that they match well with each other, especially for the peak potentials. This reveals that the cathodic peak at 1.0 V in the CV plot, ascribed to the reduction of Mn^{3+} to Mn^{2+}, is not perceptible from the 2nd cycle (and thus being considered as an irreversible reaction in many studies), while it is obviously identified at 1.07 V in the dQ/dV profiles and progressively enhanced upon cycling (discussed later). Another cathodic peak at around 0.95 V is also discerned since the 3rd cathodic scan in the dQ/dV curves, which is probably associated with the reduction of ZnO. Actually, the dQ/dV plot could reflect more defined peaks, thus providing a powerful tool to perceive weak redox conversions during the discharge/charge processes.

To better understand the conversion mechanism and the origin of the capacity increase, the differential normalized capacity versus voltage (dQ_N/dV vs V) of Cell 1 is analyzed, based on the galvanostatic discharge/charge cycling from the 26th to the 575th cycles at 500 mA/g with the capacity climbing from 440 to 910 mA·h/g. Figures 7(c) and (d) display the dQ_N/dV vs V curves for the cathodic and anodic processes, respectively. For the cathodic process, the sharp peak at the low voltage progressively moves negatively from 0.76 to 0.31 V as cycling proceeds, which is consistent with the CV result shown in Fig. 6, and indicates that the reductive conversion is triggered at a lower voltage. The inset in Fig. 7(c) shows the amplified view in a range from 0.7 to 3.0 V, as indicated by the dashed rectangle, disclosing that two well-resolved peaks centered at around 1.2 and 2.0 V are strengthening upon cycling. Their corresponding anodic peaks, shown in the anodic scans in Fig. 7(d), are at 2.2 and 2.8 V, respectively, and also grow upon cycling. Conversely, the intensities of the predominant peaks at 1.2 and 1.5 V gradually decrease as cycling proceeds. The redox pair at lower potentials (1.2/2.2 V) could be assigned to the conversion reactions of MnO and Mn_3O_4, in the light of the previous discussion. The redox pair at higher potentials (2.0/2.8 V) does not originally exist but arises during cycling, and the exact reaction mechanism is not very clear at this point. Possible interpretations are the further conversion between Mn_3O_4 and Mn_2O_3, or the reversible reaction associated with the SEI film over the surface of metal oxide nanoparticles [29−31]. Moreover, since the final phase in our study is not MnO, but Mn_3O_4 or even Mn_2O_3, the reversible theoretical capacity of the $ZnMn_2O_4/Mn_3O_4$ composite material could be modified to 919 (or 1033) mA·h/g, when considering the mass ratio of

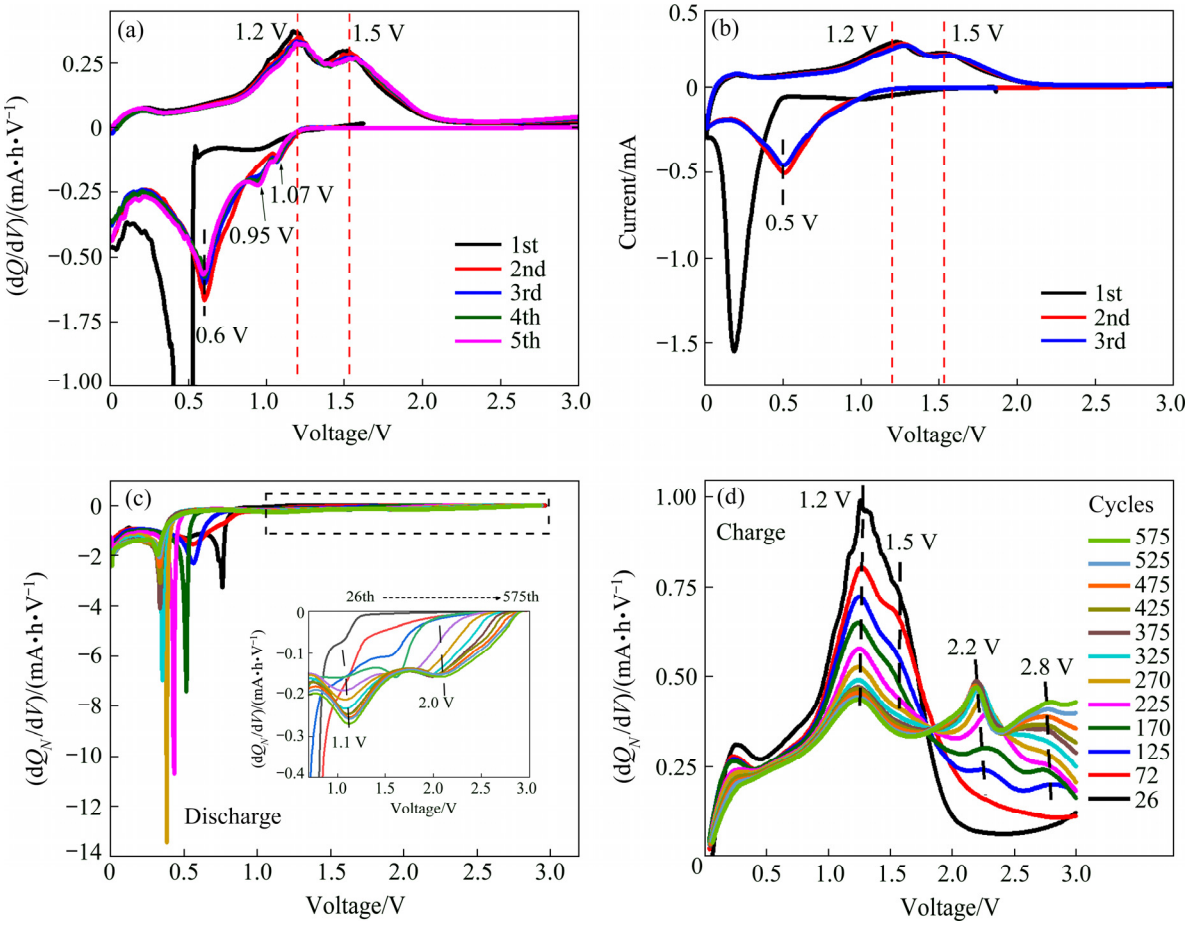

Fig. 7 The first five cycles of dQ/dV vs V profiles derived from Fig. 5(b) (a), the first three cycles of CV curves from $ZnMn_2O_4$/Mn_3O_4 half-cell (b), and differential normalized capacity dQ_N/dV vs V profiles of Cell 1 from the 26th to 575th cycle derived from galvanastatic cycling at 500 mA/g (c, d) ((c) is the cathodic scans and (d) is the anodic scans; The inset in (c) is enlarged view over voltage range from 0.7 to 3.0 V)

$ZnMn_2O_4$ to Mn_3O_4 in the composite and assuming the final phase is completely Mn_3O_4 (or Mn_2O_3). Obviously, the recalculated theoretical value of the $ZnMn_2O_4$/Mn_3O_4 composite is still lower than the measured capacity (up to 1276 mA·h/g at 100 mA·h/g). There are still other mechanisms contributing to the additional charge storage. For instance, the capacitive effect of electrode materials has been proved to contribute considerably to the discharge/charge capacity, and might even become the main contributor for the nanostructured electrode materials [29,31−33]. For example, HUANG et al [34] recently found a tremendous improvement in capacity from 993 to 2243 mA·h/g after 135 charge/discharge cycles for the electrode material of ultrathin MnO_2 sheet assembled three dimensional flower microsphere grown on nitrogen-doped graphene, and the capacitive contribution reaches 61% at the scan rate of 1 mV/s for the fresh cell, which climbs to 70% in the cycled cell.

To explain why the oxidation reaction from MnO to Mn_3O_4 in Mn-based oxides appears in some studies but not in others, we infer that the oxidation process is determined by the activation energy of the electrochemical reaction, which is usually affected by the properties of the electrode materials, including the crystallinity, phase structure, grain size, the surface property, the lithium ion and electron conductivity of the electrode materials, etc. Therefore, the activation energy is different in various studies because the Mn-based oxide materials are synthesized by various ways and show diverse nanostructures. Further, as the electrode material properties would change during the discharge/charge cycling, the

activation energy of the electrochemical conversion alters, and this could explain why the MnO/Mn_3O_4 conversion does not occur at the beginning in this work, but appears and gradually increases during the cycling. This process can be regarded as an activation process associated with the structural reorganization and phase change during the conversion reactions, the enhanced surface/interfacial reaction kinetics during cycling, and the modification in the lithium ion and electron mobility, etc [35,36]. However, in-depth studies are still needed.

4 Conclusions

(1) Hierarchical $ZnMn_2O_4/Mn_3O_4$ composite sub-microrods were synthesized via a water-in-oil microemulsion method followed with a calcination process.

(2) The $ZnMn_2O_4/Mn_3O_4$ composite electrode displayed a continuous increase in capacity with cycling and the capacity exceeded the theoretical value.

(3) CV and differential capacity analysis during the cycling process disclosed that two redox conversions were formed and strengthened during the discharge/charge cycling.

(4) The new redox conversions lead to the capacity increase, but there are still other factors contributing to the capacity increase.

Acknowledgments

Ting-ting FENG acknowledges the financial support from Professor Paul V. BRAUN at Department of Materials Science and Engineering, University of Illinois at Urbana-Champaign, and the support from Chinese Scholarship Council during her visit to University of Illinois at Urbana-Champaign, and partial financial supports from Department of Science and Technology of Sichuan Province, China (2019YFH0002, 2019YFG0222 and 2019YFG0526). The research was partly carried out in the Frederick Seitz Materials Research Laboratory Central Research Facilities, University of Illinois at Urbana-Champaign.

References

[1] SHENG Li-zhi, LIANG Shi-chuan, WEI Tong, CHANG Jin, JIANG Zi-mu, ZHANG Long-hai, ZHOU Qi-hang, ZHOU Jia-li, JIANG Li-li, FAN Zhuang-jun. Space-confinement of MnO nanosheets in densely stacked graphene: Ultra-high volumetric capacity and rate performance for lithium-ion batteries [J]. Energy Storage Materials, 2018, 12: 94−102.

[2] WANG Chang-bin, YIN Long-wei, XIANG Dong, QI Yong-xin. Uniform carbon layer coated Mn_3O_4 nanorod anodes with improved reversible capacity and cyclic stability for lithium ion batteries [J]. ACS Applied Materials & Interfaces, 2012, 4: 1636−1642.

[3] SHI Shao-jun, DENG Shi, ZHANG Ming, ZHAO Meng-xi, YANG Gang. Rapid microwave synthesis of self-assembled hierarchical Mn_2O_3 microspheres as advanced anode material for lithium ion batteries [J]. Electrochimica Acta, 2017, 224: 285−294.

[4] LI Lie-wu, WANG Li-Ping, ZHANG Ming-yu, HUANG Qi-zhong, HE Ke-jian, WU Fei-xiang. Enhancement of lithium storage capacity and rate performance of Se-modified MnO/Mn_3O_4 hybrid anode material via pseudocapacitive behavior [J]. Transactions of Nonferrous Metals Society of China, 2020, 30: 1904−1915.

[5] ZOU Min-min, AI Deng-jun, LIU Kai-yu. Template synthesis of MnO_2/CNT nanocomposite and its application in rechargeable lithium batteries [J]. Transactions of Nonferrous Metals Society of China, 2011, 21: 2010−2014.

[6] ZHANG Long-hai, ZHU Si-qi, CAO Hui, HOU Lin-rui, YUAN Chang-zhou. Hierarchical porous $ZnMn_2O_4$ hollow nanotubes with enhanced lithium storage toward lithium-ion batteries [J]. Chemistry−A European Journal, 2015, 21: 10771−10777.

[7] ZHOU Liang, ZHAO Dong-yuan, LOU Xiong-wen. Double-shelled $CoMn_2O_4$ hollow microcubes as high-capacity anodes for lithium-ion batteries [J]. Advanced Materials, 2012, 24: 745−748.

[8] HUANG Jia-rui, WANG Wei, LIN Xi-rong, GU Cui-ping, LIU Jin-yun. Three-dimensional sandwich-structured $NiMn_2O_4$@reduced graphene oxide nanocomposites for highly reversible Li-ion battery anodes [J]. Journal of Power Sources, 2018, 378: 677−684.

[9] ZHANG Yao-hui, ZHANG Yu-wen, GUO Chun-li, TANG Bin, WANG Xiao-min, BAI Zhong-chao. Porous $ZnMn_2O_4$ nanowires as an advanced anode material for lithium ion battery [J]. Electrochimica Acta, 2015, 182: 1140−1144.

[10] LIU Yu-rong, BAI Jing, MA Xiao-jian, LI Jing-fa, XIONG Sheng-lin. Formation of quasi-mesocrystal $ZnMn_2O_4$ twin microspheres via an oriented attachment for lithium-ion batteries [J]. Journal of Materials Chemistry A, 2014, 2: 14236−14244.

[11] YANG Yan-yan, ZHAO Yan-qiang, XIAO Li-fen, ZHANG Li-zhi. Nanocrystalline $ZnMn_2O_4$ as a novel lithium-storage material [J]. Electrochemistry Communications, 2008, 10: 1117−1120.

[12] KIM S W, LEE H W, MURALIDHARAN P, SEO D H, YOON W S, KIM D K, KANG K. Electrochemical performance and ex situ analysis of $ZnMn_2O_4$ nanowires as anode materials for lithium rechargeable batteries [J]. Nano Research, 2011, 4: 505−510.

[13] LOWE M A, GAO Jie, ABRUNA H D. In operando X-ray studies of the conversion reaction in Mn_3O_4 lithium battery anodes [J]. Journal of Materials Chemistry A, 2013, 1: 2094−2103.

[14] SU Hang, XU Yue-feng, FENG Shan-Cheng, WU Zhen-guo, SUN Xue-ping, SHEN Chong-heng, WANG Jian-qiang, LI Jun-tao, HUANG Ling, SUN Shi-gang. Hierarchical Mn_2O_3 hollow microspheres as anode material of lithium ion battery and its conversion reaction mechanism investigated by XANES [J]. ACS Applied Materials & Interfaces, 2015, 7: 8488−8494.

[15] JIAN Guo-qiang, XU Yun-hua, LAI Li-chung, WANG Chun-sheng, ZACHARIAH M R. Mn_3O_4 hollow spheres for lithium-ion batteries with high rate and capacity [J]. Journal of Materials Chemistry A, 2014, 2: 4627−4632.

[16] GU Xin, YUE Jie, LI Liang-jun, XUE Hai-tao, YANG Jian, ZHAO Xue-bo. General synthesis of MnO_x (MnO_2, Mn_2O_3, Mn_3O_4, MnO) hierarchical microspheres as lithium-ion battery anodes [J]. Electrochimica Acta, 2015, 184: 250−256.

[17] DENG Yuan-fu, LI Zhan-en, SHI Zhi-cong, XU Hui, PENG Feng, CHEN Guo-hua. Porous Mn_2O_3 microsphere as a superior anode material for lithium ion batteries [J]. RSC Advances, 2012, 2: 4645−4647.

[18] WANG Na-na, MA Xiao-jian, XU Hua-yun, CHEN Liang, YUE Jie, NIU Fei-er, YANG Jian, QIAN Yi-tai. Porous $ZnMn_2O_4$ microspheres as a promising anode material for advanced lithium-ion batteries [J]. Nano Energy, 2014, 6: 193−199.

[19] YUAN Chang-zhou, LI Jiao-yang, HOU Lin-rui, ZHANG Long-hai, ZHANG Xiao-gang. Template-free fabrication of mesoporous hollow $ZnMn_2O_4$ sub-microspheres with enhanced lithium storage capability towards high-performance Li-ion batteries [J]. Particle & Particle Systems Characterization, 2014, 31: 657−663.

[20] ZHANG Gen-qiang, YU Le, WU H B, HOSTER H E, LOU X W. Formation of $ZnMn_2O_4$ ball-in-ball hollow microspheres as a high-performance anode for lithium-ion batteries [J]. Advanced Materials, 2012, 24: 4609−4613.

[21] PARK S K, JIN Ai-hua, YU S H, HA J H, JANG B C, BONG S Y, WOO S H, SUNG Y E, PIAO Yuan-zhe. In situ hydrothermal synthesis of Mn_3O_4 nanoparticles on nitrogen-doped graphene as high-performance anode materials for lithium ion batteries [J]. Electrochimica Acta, 2014, 120: 452−459.

[22] LI Peng, LIU Jing-yan, LIU Yang, WANG Yu-wei, LI Zhong-tao, WU Wen-ting, WANG Yang, YIN Ling-hong, XIE Hui, WU Ming-bo, HE Xiao-jun, QIU Jie-shan. Three-dimensional $ZnMn_2O_4$/porous carbon framework from petroleum asphalt for high performance lithium-ion battery [J]. Electrochimica Acta, 2015, 180: 164−172.

[23] GAO Qian-qian, DAI Yu-qiang, LI Cheng-bo, YANG Li-guo, LI Xiang-chang, CUI Chao-jun. Correlation between oxygen vacancies and dopant concentration in Mn-doped ZnO nanoparticles synthesized by co-precipitation technique [J]. Journal of Alloys and Compounds, 2016, 684: 669−676.

[24] KIM J G, LEE S H, KIM Y, KIM W B. Fabrication of free-standing $ZnMn_2O_4$ mesoscale tubular arrays for lithium-ion anodes with highly reversible lithium storage properties [J]. ACS Applied Materials & Interfaces, 2013, 5: 11321−11328.

[25] ZHOU L, WU H B, ZHU T, LOU X W D, Facile preparation of $ZnMn_2O_4$ hollow microspheres as high-capacity anodes for lithium-ion batteries [J]. Journal of Materials Chemistry, 2012, 22: 827−829.

[26] DUNCAN H, COURTEL F M, ABU-LEBDEH Y. A study of the solid-electrolyte-interface (SEI) of $ZnMn_2O_4$: A conversion-type anode material for Li-ion batteries [J]. Journal of The Electrochemical Society A, 2015, 162: 7110−7117.

[27] DJURFORS B, BROUGHTON J N, BRETT M J, IVEY D G. Electrochemical oxidation of Mn/MnO films: Mechanism of porous film growth [J]. Journal of The Electrochemical Society A, 2006, 153: 64−68.

[28] GUO Yu-ping, FENG Ting-ting, YANG Jian, GONG Feng, CHEN Cheng, XU Zi-qiang, HU Ce-rui, LENG Song-ming, WANG Jun-chao, WU Meng-qiang. MOF-derived manganese monoxide nanosheet-assembled microflowers for enhanced lithium-ion storage [J]. Nanoscale, 2019, 11: 10763−10773.

[29] LARUELLE S, GRUGEON S, POIZOT P, DOLLé M, DUPONT L, TARASCON J M. On the origin of the extra electrochemical capacity displayed by MO/Li cells at low potential [J]. Journal of The Electrochemical Society A, 2002, 149: 627−634.

[30] COURTEL F M, DUNCAN H, ABU-LEBDEH Y, DAVIDSON I J. High capacity anode materials for li-ion batteries based on spinel metal oxides AMn_2O_4 (A=Co, Ni, and Zn) [J]. Journal of Materials Chemistry, 2011, 21(27): 10206−10218.

[31] SU Li-wei, ZHONG Yi-ren, ZHOU Zhen. Role of transition metal nanoparticles in the extra lithium storage capacity of transition metal oxides: A case study of hierarchical core-shell Fe_3O_4@C and Fe@C microspheres [J]. Journal of Materials Chemistry A, 2013, 1: 15158−15166.

[32] BREZESINSKI T, WANG J, TOLBERT S H, DUNN B. Ordered mesoporous α-MoO_3 with iso-oriented nanocrystalline walls for thin-film pseudocapacitors [J]. Nature Materials, 2010, 9: 146−151.

[33] WANG J, POLLEUX J, LIM J, DUNN B. Pseudocapacitive contributions to electrochemical energy storage in TiO_2 (anatase) nanoparticles [J]. The Journal of Physical Chemistry C, 2007, 111: 14925−14931.

[34] HUANG Shi-fei, TIE Da, WANG Miao, WANG Bo, JIA Peng, WANG Qing-ie, CHANG Guo-liang, ZHANG Jiu-jun, ZHAO Yue-feng. Largely increased lithium storage ability of mangnese oxide through a continuous electronic structure modulation and elevated capacitive contribution [J]. ACS Sustainable Chemistry & Engineering, 2019, 7: 740−747.

[35] SUN Xiao-lei, SI Wen-ping, LIU Xiang-hong, DENG Jun-wen, XI Li-xia, LIU Li-feng, YAN Cheng-lin, SCHMIDT O G. Multifunctional Ni/NiO hybrid nanomembranes as anode materials for high-rate Li-ion batteries [J]. Nano Energy, 2014, 9: 168−175.

[36] BALAYA P, BHATTACHARYYA A J, JAMNIK J, ZHUKOVSKII Y F, KOTOMIN E A, MAIER J. Nano-ionics in the context of lithium batteries [J]. Journal of Power Sources, 2006, 159: 171−178.

微乳液法制备锂离子电池用 $ZnMn_2O_4/Mn_3O_4$ 亚微米棒及其转化反应机理

冯婷婷，杨 俭，代思忆，王俊超，吴孟强

电子科技大学 材料与能源学院，成都 611731

摘 要：采用油包水微乳液法再经煅烧制备分级 $ZnMn_2O_4/Mn_3O_4$ 复合亚微米棒。$ZnMn_2O_4/Mn_3O_4$ 电极在 550 次连续放电/充电循环中，在 500 mA/g 充放电电流条件下，其比容量从 440 mA·h/g 增加到 910 mA·h/g，并在 100 mA/g 下提供 1276 mA·h/g 的超高比容量，远高于 $ZnMn_2O_4$ 或 Mn_3O_4 的理论比容量。采用循环伏安法和微分容量分析法研究这种现象的潜在机制，两者均揭示在充放电循环过程中新的可逆氧化还原反应的产生和增强。这种新的可逆转化反应可能是由于电极材料在循环过程中的活化过程引起的，从而解释电极材料容量在循环过程中不断上升的现象；而容量超过理论值表明还有其他因素对容量的增长起作用。

关键词：$ZnMn_2O_4/Mn_3O_4$ 亚微米棒；微乳液；转化反应机理；循环伏安法；微分容量分析

(Edited by Xiang-qun LI)